



OPEN

A clinically annotated post-mortem approach to study multi-organ somatic mutational clonality in normal tissues

Tom Luijts^{1,2,3}, Kerryn Elliott³, Joachim Tetteh Siaw^{1,2,3}, Joris Van de Velde¹, Elien Beyls¹, Arne Claeys^{1,2}, Tim Lammens^{2,4,5}, Erik Larsson³, Wouter Willaert¹, Anne Vral^{1,2} & Jimmy Van den Eynden^{1,2}✉

Recent research on normal human tissues identified omnipresent clones of cells, driven by somatic mutations known to be responsible for carcinogenesis (e.g., in *TP53* or *NOTCH1*). These new insights are fundamentally changing current tumor evolution models, with broad oncological implications. Most studies are based on surgical remnant tissues, which are not available for many organs and rarely in a pan-organ setting (multiple organs from the same individual). Here, we describe an approach based on clinically annotated post-mortem tissues, derived from whole-body donors that are routinely used for educational purposes at human anatomy units. We validated this post-mortem approach using UV-exposed and unexposed epidermal skin tissues and confirm the presence of positively selected *NOTCH1/2*-, *TP53*- and *FAT1*-driven clones. No selection signals were detected in a set of immune genes or housekeeping genes. Additionally, we provide the first evidence for smoking-induced clonal changes in oral epithelia, likely underlying the origin of head and neck carcinogenesis. In conclusion, the whole-body donor-based approach provides a nearly unlimited healthy tissue resource to study mutational clonality and gain fundamental mutagenic insights in the presumed earliest stages of tumor evolution.

Spontaneously occurring somatic mutations accumulate in the genome of dividing cells during ageing. Most of these mutations are harmless, but occasionally, they lead to a cellular fitness advantage, resulting in positive selection and clonal expansion. The progressive accumulation of these driver mutations can lead to malignant tumor formation, often many decades after the occurrence of the first driver event^{1,2}. International efforts like The Cancer Genome Atlas (TCGA) and International Cancer Genome Consortium (ICGC) led to the identification of these genomic alterations in most primary tumor types. In contrast, less is known about the earliest initiating events, which are expected to occur in normal cells.

Mutational clonality in normal tissues was first shown for *TP53* in the UV-exposed skin using immunohistochemical techniques³. However, it took more than 20 years and the development of advanced Next-Generation Sequencing (NGS) techniques before these findings could be extended to other cancer genes and tissue types. In their pioneer study, *Martincoren et al.* used a deep (500×) targeted sequencing approach on 74 genes in 4 subjects and demonstrated that 18–32% of all UV-exposed epidermal skin cells are microscopic mutant clones, clusters of epithelial cells that are driven by point mutations in cancer genes commonly found in squamous cell carcinoma (SCC) skin cancer, such as *TP53* and *NOTCH1*⁴. These findings were later confirmed in healthy esophageal tissues, where age- and smoking-dependent mutational clonality was demonstrated in genes known to be involved in esophageal squamous cell carcinoma (ESCC)^{5,6}. Recently, similar DNA-based studies were performed on non-tumoral colorectal^{7,8}, uterine^{9,10}, liver^{11,12}, lung¹³ and urothelial tissues^{14,15} and an indirect RNA-based approach found clonal expansion in several healthy tissue types¹⁶. The high frequency and large size of these clones is striking, as illustrated by *NOTCH1*-driven clones in ESCC. These results suggest that some

¹Department of Human Structure and Repair, Ghent University, Ghent, Belgium. ²Cancer Research Institute Ghent, Ghent, Belgium. ³Department of Medical Biochemistry and Cell Biology, Institute of Biomedicine, The Sahlgrenska Academy, University of Gothenburg, Gothenburg, Sweden. ⁴Department of Internal Medicine and Pediatrics, Ghent University, Ghent, Belgium. ⁵Department of Pediatric Hematology-Oncology and Stem Cell Transplantation, Ghent University Hospital, Ghent, Belgium. ✉email: jimmy.vandeneynden@ugent.be

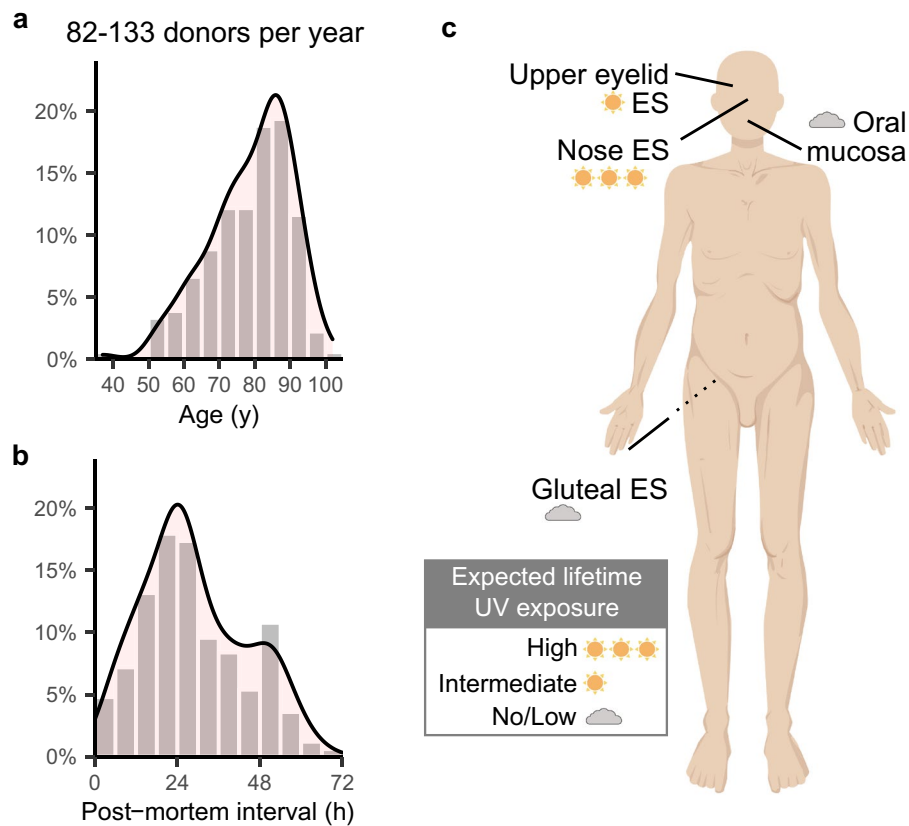


Figure 1. Detecting mutational clonality in post-mortem epithelial tissues derived from whole-body donors. (a,b) Histograms showing the distribution of (a) age and (b) post-mortem interval in the complete population of whole-body donors at the UGent Anatomy and Embryology unit (data 2016–2021). (c) Skin and oral tissues were sampled from 4 different locations as indicated.

genes favor the initial clonal expansion in normal tissues without the risk of further evolution into cancer¹⁷. Furthermore, clones with different carcinogenic potential might compete for space, especially within aging tissues^{18,19}. These new carcinogenic insights also have major translational relevance. They could even imply that therapeutically targeting genes like *NOTCH1* might increase the risk of malignant transformation by tackling benign rather than malignant clones, and opposite therapeutic approaches should be considered. Additionally, the implications for diagnostic strategies based on e.g., circulating tumor cells or cell-free DNA are to be determined. There is also a non-oncological significance as mutational clonality has been suggested to contribute to aging and other human diseases^{12,20}. In this regard it has been shown that mutational clonality in blood cells has a negative, cancer-independent impact on lifespan, likely related to an increased incidence of cardiovascular diseases²¹.

An important limitation for future studies is the lack of clinically annotated normal tissue availability. Current studies are mostly based on remnant tissues, obtained from surgical procedures. This approach is not feasible for all tissues and a drawback is the lack of comparability between different organs when samples are not obtained from the same patient. In this study, we describe an approach based on post-mortem tissues obtained from whole-body donors. Using deep targeted sequencing, we demonstrate UV-induced genomic alterations and confirm positive selection of somatic mutations in *TP53* and *NOTCH1* in epidermal skin tissues. Our study also provides the first evidence for smoking-induced somatic alterations in oral tissues. The newly developed approach potentiates future studies focusing on multi-organ genomic effects of cancer risk factors and mutagens (e.g., smoking, radiotherapy, chemotherapy), providing a valuable tool to study human carcinogenesis and other age-related diseases.

Results

A whole-body donor-based approach to study mutational clonality. On average 101 bodies are voluntarily donated to the Ghent University Anatomy and Embryology Unit each year (data 2016–2021; range 82–133). The median age of these whole-body donors is 81 years (range 36–106 years; Fig. 1a) and the majority (53%) deceased between 12 and 36 h prior to arrival (post-mortem interval; PMI), with 92% of all donors having a PMI below 72 h (Fig. 1b). They are primarily used for medical and surgical training purposes^{22,23}, but also provide a rich normal tissue resource to study clonal changes in different organs of the human body.

To demonstrate the feasibility of such a post-mortem tissue-based mutational clonality detection platform, we developed a 4-step methodology (Fig. S1a). In a first step, skin and oral tissues were sampled and relevant clinical information (i.e., age, gender, smoking status, oncological history) as well as the PMI was recorded by

the responsible physician. The choice for skin tissues for initial evaluation purposes was motivated by their easy accessibility, high expected UV-induced mutation rates (with negative controls from unexposed regions) and knowledge of the expected (positive control) results from earlier studies⁴. Secondly, 5 mm (diameter) punch biopsies were taken (surface area 19.63 mm²), and the epithelial layer was enzymatically isolated. In a third step DNA was extracted, DNA concentrations and integrity were determined, and samples were sequenced. Importantly, we did not observe any PMI-dependent DNA degradation, as evaluated using gel electrophoresis (eyelid samples in 10 subjects with PMI between 6 and 83 h evaluated, Fig. S1b). In a fourth step, somatic mutations were called, followed by an analysis of clone sizes, mutational signatures, and positive selection signals.

We aimed to validate our approach using 2 largely orthogonal approaches: (1) by identifying positive selection of somatic mutations in cancer genes and (2) by demonstrating UV-specific alterations in UV-exposed skin. To achieve this, we sampled skin and oral tissues from 2 different donors: a 94-year-old, male, non-smoking donor (subject PM01, PMI 33 h) and a 90-year-old, male donor (subject PM02, PMI 38 h) with a smoking history (1 package a day between the age of 18 and 38, as derived from the medical record). To explore the effects of different expected lifetime UV exposure, skin samples were taken at 3 locations: bridge of the nose (high UV exposure), upper eyelid (intermediate UV exposure) and gluteal region (no/low UV exposure). Additional non-UV-exposed oral mucosa samples were taken from the inner buccal region (Fig. 1c).

Somatic mutations in known driver genes are detectable in post-mortem tissues. Deep (1000×) sequencing was performed, targeting the coding regions of 153 genes. Apart from 76 earlier defined skin cancer driver genes (oncogenes or tumor suppressor genes), this gene panel also contained (1) 25 additional driver genes that have been associated to skin or head and neck cancer, (2) 20 housekeeping genes that were used as a negative control in our study (no selection signals or clonality expected) and (3) 32 genes that are putatively involved in immune evasion, which are further referred to as “immune genes” (see “Methods” and Table S1 for details). After alignment, somatic mutations were called using *Shearwater ML*, an algorithm that is optimized for the detection of low frequency variants from deep targeted sequencing data. We retrieved 910 somatic mutations with an average variant allele frequency (VAF) of 0.011 and ranging between 0.0023 and 0.11 (Fig. S1c, Table S1).

The 5 most frequently mutated genes were *NOTCH1* (6.6 average mutations per sample; mps), *TP53* (3.1 mps), *MUC17* (2.5 mps), *FAT1* (2.2 mps) and *APOB* (2.1 mps). Most samples contained multiple mutations in these genes, and remarkably, *NOTCH1* mutations were identified in all samples (between 1 and 16 different *NOTCH1* mutations per sample). Overall, we identified somatic mutations in 119 different genes, including *NOTCH2* (1.6 mps, 6th most frequently mutated gene) and *NOTCH3* (0.82 mps), genes that have been previously identified as clonal drivers in healthy skin (Fig. 2).

Most of these mutations were observed in the 101 driver genes (93%, 844 mutations). The majority of the remaining mutations occurred in the 32 immune genes (5%, 46 mutations), while 20 mutations (2%) were observed in the 20 housekeeping control genes (Fig. S2, Table S1).

Clonal alterations in epidermal skin and oral mucosa are primarily driven by *NOTCH1* and *TP53*. The large difference between the number of mutations observed in driver versus housekeeping genes suggests positive selection acting on the former. To confirm this, we first focused on the global ratio of nonsynonymous over synonymous mutations. In skin samples, this ratio was higher than the expected ratio, as derived from a random mutation background model (3.68 versus 2.12 respectively; $P = 3.7e-08$). This higher observed to expected mutation ratio (i.e., global dN/dS = 1.73) suggests that 42% (0.73/1.73) of the identified nonsynonymous mutations have been subjected to positive selection forces (Fig. 3a). Significant selection signals (i.e., dN/dS values above 1) were solely observed in the group of driver genes (dN/dS = 1.78, $P = 2.4e-08$), and not in the immune genes (dN/dS = 0.81, $P = 0.72$) nor the housekeeping genes (dN/dS = 0.65, $P = 0.81$; Fig. 3b). Additionally, signals were stronger for nonsense mutations (dNons/dS = 3.04, $P = 3.9e-09$) than for missense mutations (dMiss/dS = 1.80, $P = 6.3-09$) and were also present in the oral samples (dN/dS = 2.13, $P = 1.3e-04$; Fig. 3a,b, Table S1). When focusing on single genes in skin, we observed significant selection signals (at 10% FDR) in *NOTCH1*, *TP53* and *FAT1* (Figs. 3a, S3a).

Because selection pressures are mainly expected on nonsynonymous mutations with high mutational impact, we also compared PolyPhen-2 (PP2) mutational impact scores between observed and expected mutations. Higher PP2 scores were observed for our set of somatic mutations (median PP2 = 0.50) as compared to the expected scores (median PP2 = 0.11; $P = 2.3e-09$; Fig. 3c). Like the dN/dS approach, this difference was only observed for driver genes ($P = 3.5e-07$) and not for the other gene sets (Fig. 3d). We confirmed positive selection signals (at 10% FDR) in skin tissues in *NOTCH1*, *TP53* and *FAT1* and, additionally, also found significant signals in *NOTCH2*, *CDKN2A*, *BCORL1* and *AJUBA* (Figs. 3c, S3b). In oral tissues, positive selection was detected in *NOTCH1*, *FAT1*, *TP53* and *NOTCH2* (Fig. 3c).

Our results confirm earlier reports on somatic driver mutation clonality in healthy skin. Based on the variant allele frequency and biopsy size, we imputed the clone sizes for the genes that were identified to be under positive selection and found 78 clones per cm² skin (35 *NOTCH1*, 16 *TP53*, 15 *FAT*, 6 *NOTCH2*, 2 *BCORL1*, 2 *CDKN2A* and 2 *AJUBA* clones; Fig. 4a,b). *BCORL1*-driven clones had the largest size (median 0.49 mm²) while the smallest clone sizes were found for *FAT1* (0.23 mm²; Fig. 4a,c). These clone sizes were larger than described previously⁴, although the total percentage of skin occupied by the most abundant clones was largely comparable between both studies, with 15.2% of skin cells estimated to contain *NOTCH1* mutations, 5.7% *TP53* mutations, 4.7% *FAT1* mutations and 2.1% *NOTCH2* mutations (Fig. 4d). In the oral mucosa, similar clonal densities were observed for the donor with the smoking history, but not for the non-smoking donor, where clones were relatively scarce (Fig. S4).

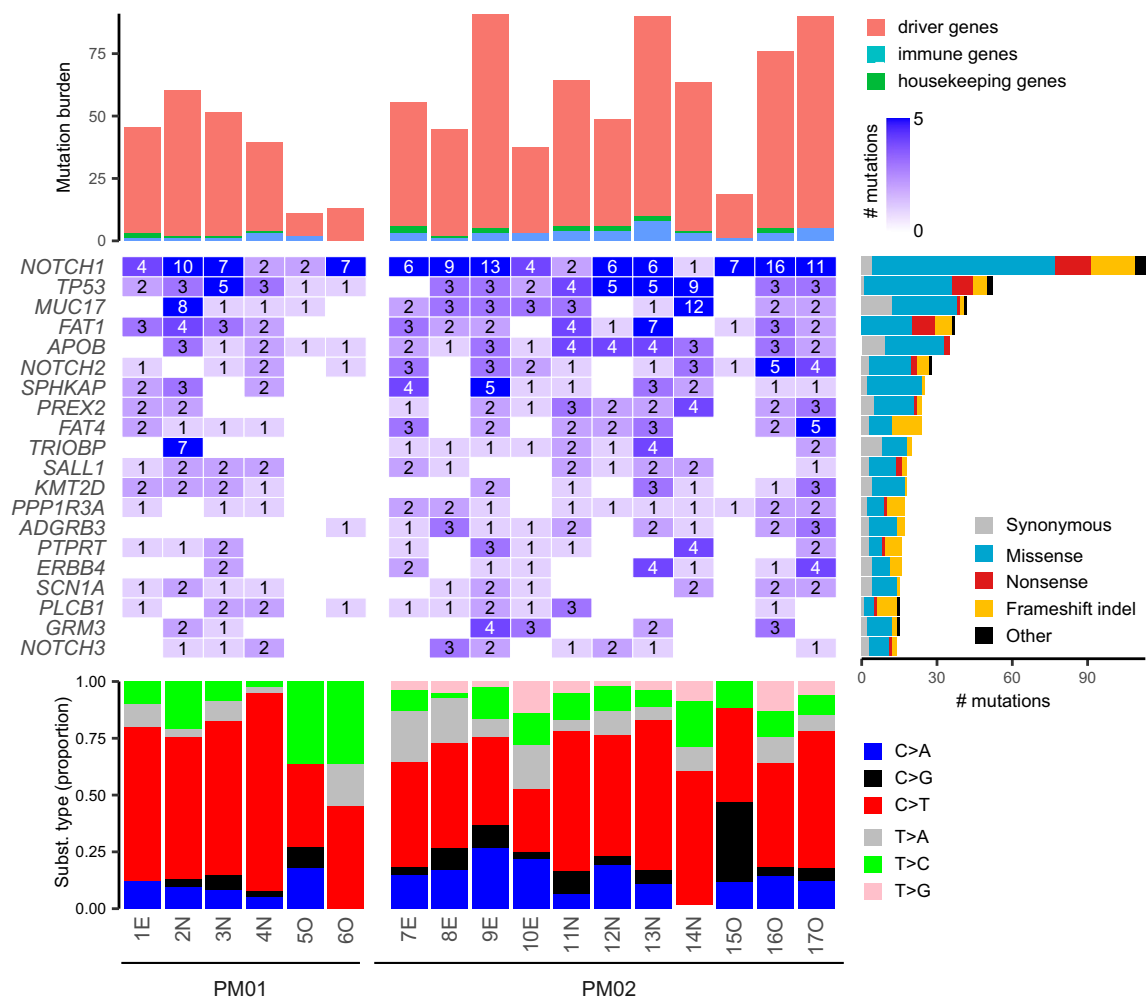


Figure 2. Characterization of somatic mutations in epidermal skin and oral epithelia. Somatic mutations were called from deep (1000 \times) targeted sequencing. The 20 most frequently mutated genes with indication of the number of identified mutations per sample are shown in the middle plot. Genes are ranked from top to bottom following mutation frequency, as indicated by the right bar. Upper plot shows the mutation burden, stacked according to the type of gene (driver gene, immune gene or housekeeping gene, as indicated). Bottom plot shows the distribution of the 6 main substitution types in each sample. Sample and patient pseudo-identifiers indicated on the bottom. E, epidermal eyelid sample; N, epidermal nose sample; O, oral sample.

UV-specific genomic alterations in epidermal skin correlate to the expected amount of lifetime UV exposure. As an additional validation of our approach, we aimed to detect UV-induced genomic changes in post-mortem tissues derived from whole-body donors. The substitutions in the 12 skin samples were predominated by C>T mutations (56%; Figs. 2, 5a). Contrary to the other 5 substitution types and as expected for UV-induced somatic mutations, these C>T mutations mainly occurred in a dipyrimidine context (88%) and were 24% more prevalent in the coding strand than the template strand ($P=0.054$, exact Poisson test), suggesting transcriptional strand bias (Fig. 5a). This mutational pattern is consistent with previous UV exposure, which was further confirmed by the strong predominance (82.4%) of coding strand-specific CC>TT dinucleotide variants (DNVs; $P=3.4\text{e-}10$; Fig. 5b) and similarity of the samples' 96 trinucleotide substitution type signature (i.e., substitution type and adjacent base pairs) with the well-known UV-associated single base substitution signature (SBS) 7 (Fig. 5c). This signature was found in all skin samples (mean contribution 39.3% per sample) and was the most prevalent signature in 10/12 skin samples. Interestingly, the smoking-related signature 4 was retrieved in 7/11 samples from subject PM02, which was known to have a smoking history (Fig. 5c).

To exclude that this putative UV signal was biased by the rather limited genomic coverage of our gene panel and/or positive selection processes, we extended our analysis to known UV hotspots in the promoter regions of *RPL13A* and *DPH3*. Here, C>T mutations occurring in a CTTCCGG sequence context have previously been associated with the amount of cumulative UV-exposure, as the binding of the ETS transcription factor to this motif increases susceptibility to pyrimidine dimer formation^{24,25}. We sequenced these regions using an error-correcting amplicon sequencing protocol (SiMSen-Seq) and detected UV-specific mutations in the UV-exposed eyelid and nose samples, but not in the non-exposed gluteal or oral samples (Fig. 5d,e, Table S1). Further, the variant allele frequency (VAF) was significantly higher in nose samples than eyelid samples, in line with the

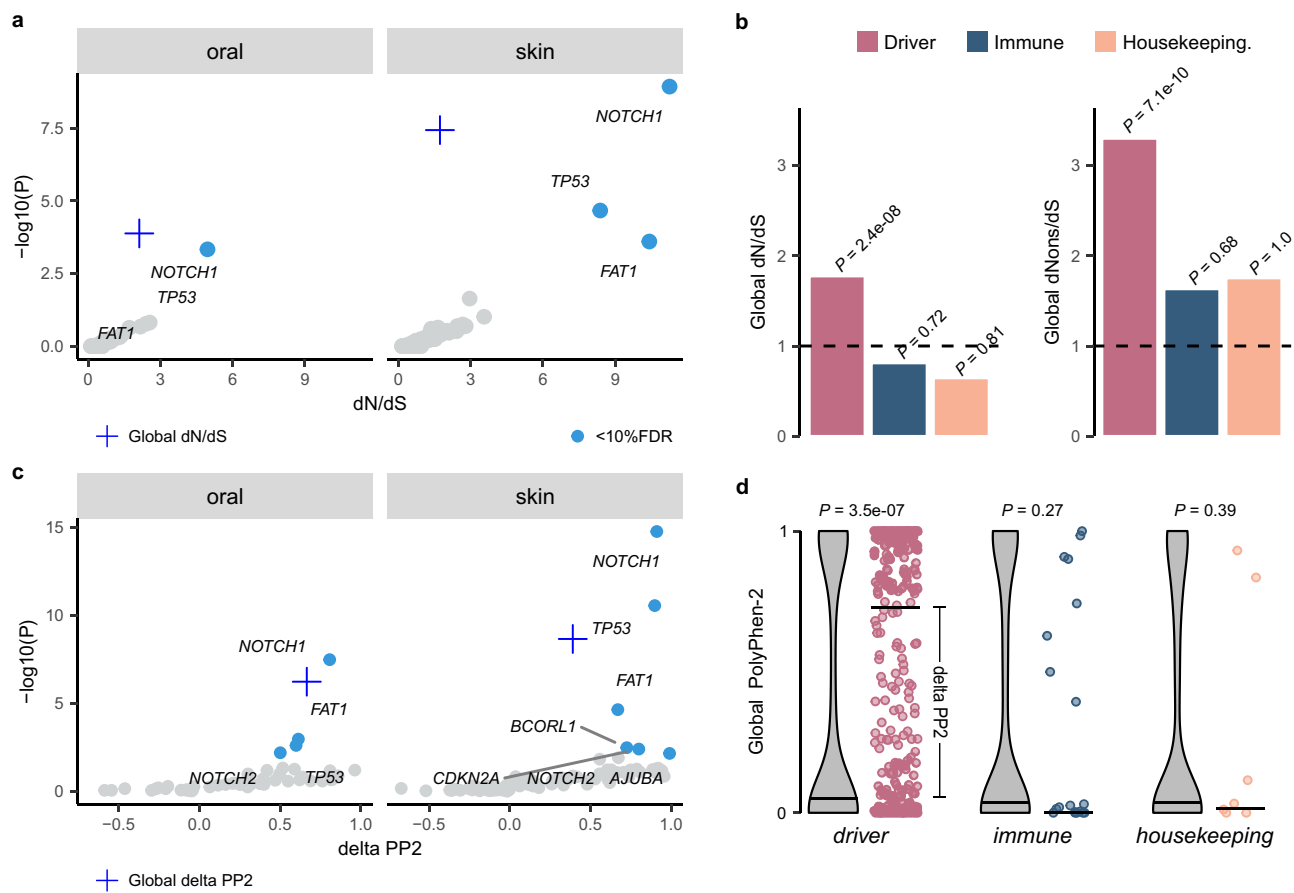


Figure 3. Positive selection signals in driver mutations in oral and skin epithelial tissues. **(a,b)** Analysis of the number of substitutions. dN/dS and dNons/dS values calculated by normalization to the expected number of sites and P values calculated using a one-sided binomial test (“Methods”). **(a)** Scatter plot with dN/dS values on the x-axes and (\log_{10} -transformed) P values on the y-axes. Genes containing significant dN/dS values (at 10% FDR) indicated in blue. Global dN/dS value indicated by plus-sign. **(b)** Barplot showing global dN/dS or global dNons/dS for driver, immune and housekeeping gene sets as indicated. **(c,d)** Analysis of the PolyPhen-2 (PP2) functional impact scores. For each gene, PP2 scores were compared with their expected value as simulated in the absence of any selection pressure (“Methods”). P values calculated using a one-sided Wilcoxon rank sum test. **(c)** Scatter plot with skin delta PP2 (difference between median observed and expected values, as illustrated in panel d) on the x-axes and P values on the y-axis. Genes with significant differences (at 10% FDR) indicated in blue. **(d)** Plots showing expected (violin plot) and observed (scatter plots) PP2 values for skin driver, immune and housekeeping gene sets as indicated. Median values indicated by horizontal lines.

higher expected lifetime UV exposure of the former ($P = 9.0 \times 10^{-3}$, two-sided Student’s T-Test; Fig. 5e). These results confirm that low frequency UV-induced mutations can be accurately detected in post-mortem skin tissues.

Discussion

Omnipresent clones of mutated cells have been identified in epithelia from different organs²⁶. These clones are driven by somatic mutations known to be involved in human carcinogenesis. New insights are changing our current understanding of (early) tumor evolution and have putative implications for cancer diagnostics and treatment, but further research is hampered by the rather limited availability of clinically annotated normal tissues. In this study, we have demonstrated that post-mortem tissues, derived from whole-body donors, could provide a nearly unlimited human tissue resource for future studies.

We validated our methodology on epidermal skin, a tissue where mutational clonality has been well-characterized and UV light is known to be an important mutagen. Firstly, we confirmed earlier findings on driver gene clonality. We found positive selection signals in *NOTCH1-2*, *TP53* and *FAT1*, demonstrating that these cancer genes are responsible for clonal alterations in healthy skin. While the estimated proportion of healthy skin cells containing these mutations (e.g., 15% *NOTCH1* mutations and 5% *TP53* mutations) was remarkably similar to previous reports based on either targeted sequencing approaches⁴ or immunohistochemistry³, the inferred clonal sizes and frequencies (number per cm^2) were respectively higher and lower than reported previously. This is likely related to a lower sensitivity to detect small clones due to the larger punch biopsy sizes that were used in this study (5 mm diameter vs. 1–2 mm in previous reports⁴). Indeed, assuming a minimal VAF detection threshold of 0.5% implies detectable clones of 19.6 mm^2 , 3.1 mm^2 and 0.79 mm^2 for 5 mm, 2 mm, and 1 mm

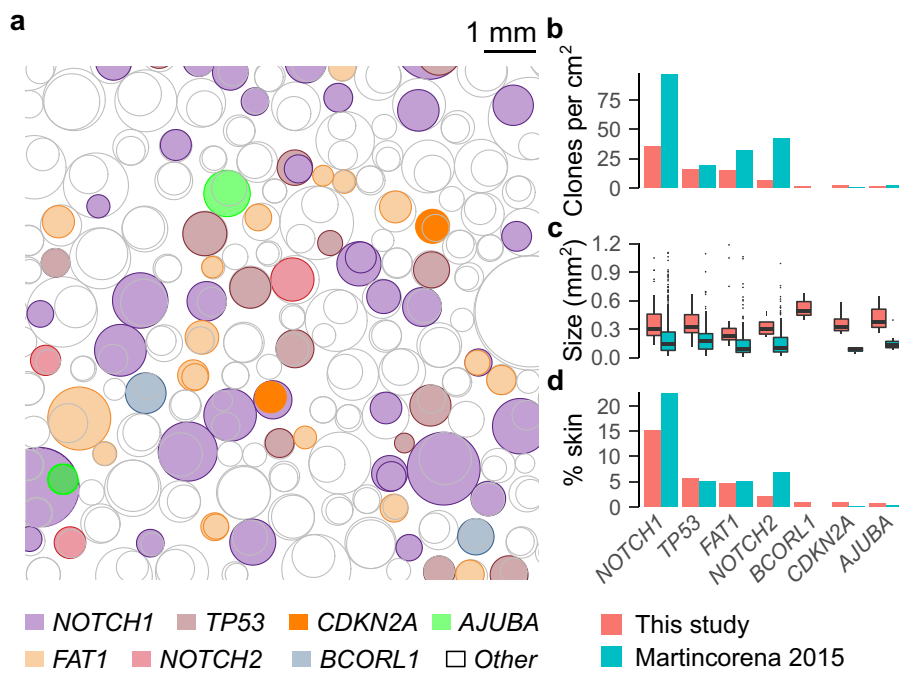


Figure 4. Clonal alterations in healthy UV-exposed skin. **(a)** Visualization of the estimated number and size of somatic mutation-driven clones in 1 cm^2 healthy skin. Data from PM01 and PM02 pooled. Clones driven by genes for which positive selection signals were found in this study are colored as indicated in bottom legend. Other clones are uncolored. Clones were positioned randomly with clone sizes and frequency based on data from this study. **(b-d)** Comparison of **(b)** clone frequency (number per cm^2), **(c)** clone size and **(d)** estimated percentage of skin occupied by each clone between this study and the study from *Martincorena* 2015 for genes for which positive selection signals were found.

punch biopsies, respectively. The theoretical advantage of larger punch biopsy sizes is the higher sensitivity to detect lowly frequent large clones. This could explain the additional identification of positive selection signals in *CDKN2A*, *BCORL1* and *AJUBA*. *CDKN2A* is a well-known tumor suppressor gene in several cancer types, including SCC²⁷. *AJUBA* is a regulator of epidermal homeostasis and has been implicated in SCC as well^{27,28}. Less is known about *BCORL1* (BCL6 corepressor like 1). Somatic mutations in this transcriptional corepressor have been identified in hematological malignancies²⁹ and, interestingly, have been reported to be associated with resistance to *BRAF* inhibition treatment in melanoma³⁰.

As a second validation approach, we confirmed UV-specificity of the identified genomic alterations in healthy skin. As expected, UV-exposed skin samples were characterized by a high amount of C>T single nucleotide mutations that occurred in pyrimidine dimers and were more frequent on the coding than the template strand. This transcriptional strand bias was most pronounced in the abundant CC>TT dinucleotide substitutions in skin. Further sequencing of 2 promoter regions that are known to be specifically altered by UV mutagenesis provided final confirmation.

Genomic immune evasion mechanisms (e.g., *B2M* mutations, *HLA* deletions) are relatively frequent in primary tumors^{31,32} and indirect evidence suggests their occurrence early during tumor evolution³³, but this has never been shown directly. Therefore, we included a panel of genes in which somatic mutations have been suggested to result in immune evasion. We identified 46 mutations in these genes, but no selection signals were found. Larger studies are required to determine whether immune surveillance and evasion have any influence on epidermal skin clonality.

One of the donors we sequenced was a former smoker, information that was derived from the medical record. Interestingly, we identified the cigarette smoke related mutational signature SBS4 in most samples from this patient. Remarkably, this mutational signature was not restricted to the oral mucosa (where it is expected) but was also retrieved in facial skin samples. To our knowledge, these smoking-induced somatic mutations in healthy skin have not been identified previously. They could be related to the higher squamous skin cancer risk reported in smokers³⁴, although no final conclusions are possible at this stage due to (1) the limited sample size of our study and (2) the rather limited genomic coverage of the gene panel with relatively large numbers of substitutions demonstrated to be under positive selection. Nevertheless, these findings clearly demonstrate the potential of a clinically annotated whole-body based approach to study somatic mutations in healthy skin.

Our study was restricted to epidermal skin and oral mucosa samples. Sampling at other locations could pose additional challenges, particularly for organs that are less accessible (e.g., pancreas, brain). The longer dissection

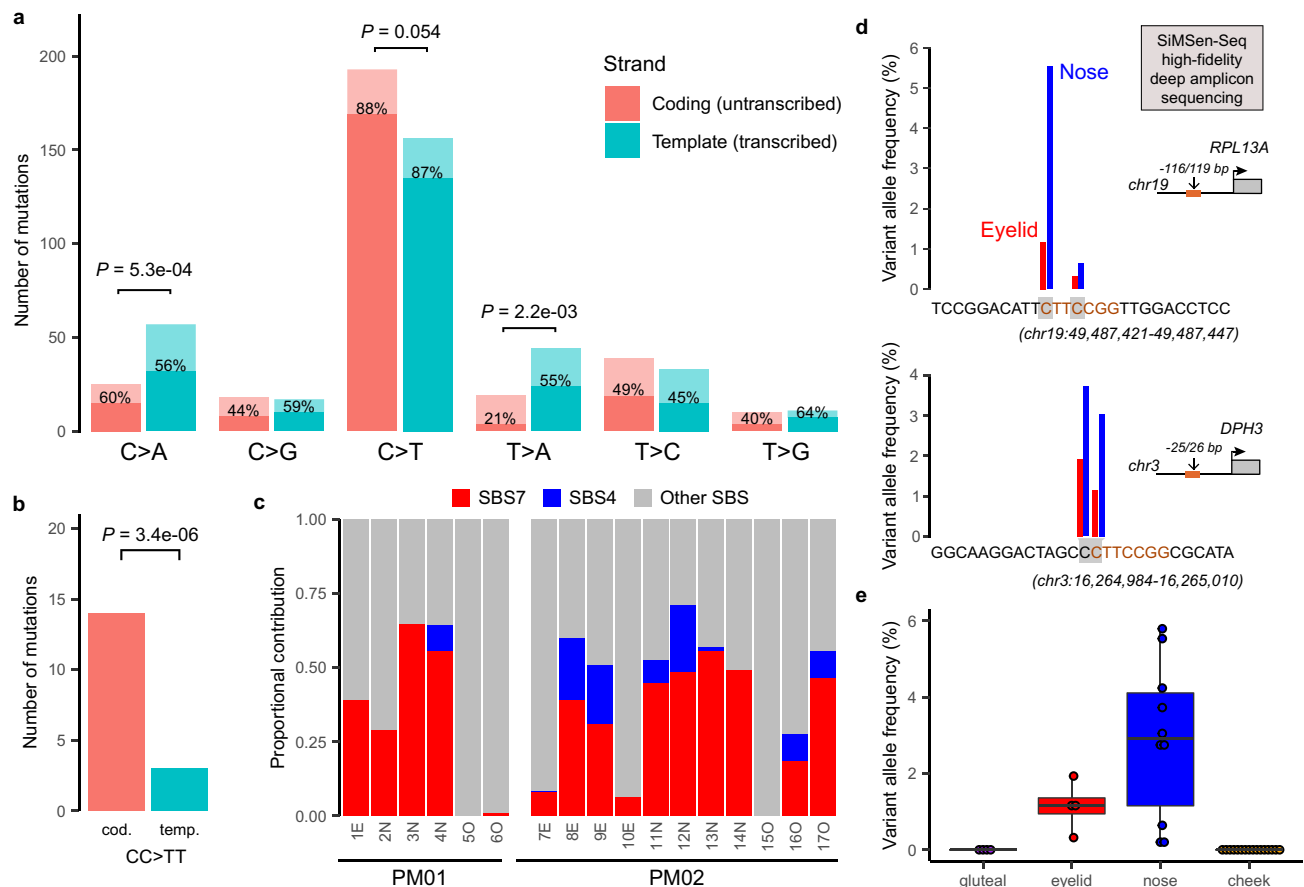


Figure 5. Detection of UV-induced somatic mutations in post-mortem epithelial tissues. **(a–c)** Deep (1000×) targeted sequencing results. **(a,b)** Bar plots representing the total number of single nucleotide variants (a) or dinucleotide variant (DNVs; b), detected in epidermal skin (12 samples). Substitutions are stratified according to the occurrence of the pyrimidine on the coding (untranscribed) or template (transcribed) strand as indicated. Transcriptional strand bias tested using Poisson exact test. Bars are colored by strand as indicated and following the number of substitutions occurring in a dipyrimidine (dark, % indicated) or other sequence (light) context. **(c)** Proportion of known mutational signatures retrieved by analyzing the cosine similarity between the distribution of 96 trinucleotide substitution types and 30 known COSMIC mutational signatures. Single base substitution signatures (SBS) 4 and 7 colored as indicated. **(d,e)** SiMSen sequencing of well-known UV hotspot mutations in *RPL13A* and *DPH3* promoters. **(d)** Data from PM02 for illustration, 2 hot spots each as indicated by grey shaded nucleotides, sequence indicated in orange. **(e)** Boxplot summarizes results for both study subjects, all hotspots and sample locations as indicated. Boxplot indicates median values and lower/upper quartiles with whiskers extending to 1.5× the interquartile range. Dots show individual data points.

times required for these organs could result in longer PMIs, possibly affecting tissue isolation procedures and DNA integrity. This remains to be determined.

Mutational clonality has been studied in post-mortem tissues derived from autopsy subjects³⁵. Relatedly, pan-organ sampling during autopsies was recently used for embryonic cell lineage tracing based on somatic mutations shared across different organs^{36–38}. However, in contrast to donor-based approaches, autopsies imply less control over the inclusion of subjects of interest. This could be particularly relevant in (large) future studies that aim to determine how human disease is directed by clonal changes¹² or how (iatrogenic) mutagens such as chemotherapy or radiotherapy influence driver mutational clonality in multiple organs. Our approach provides the opportunity to include subjects of interest by screening medical records upon donor arrival. Given the relatively high prevalence of oncological or cardiovascular diseases at the time of death, the inclusion of relatively large study populations is very realistic, especially when donor data from different human anatomy departments are merged as part of larger whole-body biobanking efforts.

Methods

Study subjects and ethics. Ten whole-body donors were included in this study between January 2020 and November 2021. Relevant clinical information (smoking status, oncological history, including chemo- and or radiotherapy) was derived from the medical record by the responsible physician from the Ghent University Center for Training and Research in Anatomical Sciences (CETRAS). Together with age, gender, sampling date and the post-mortem interval (PMI, defined as the difference between recorded time of death and sampling time), this clinical information was recorded and linked to the samples using a pseudonym (PM01, ...). After

sampling, subjects were embalmed and used for surgical training and educational purposes as part of the normal routine at the Anatomy and Embryology unit.

The study was carried out in accordance with the Declaration of Helsinki for experiments involving humans and was approved by the ethical committee of Ghent University Hospital (2019/1789). All donors gave written informed consent for body donation prior to death.

Sampling, epithelial tissue isolation and DNA extraction. Small 1–2 cm² tissue biopsies were taken by experienced anatomists from 3 skin locations (upper eyelid, nose bridge and gluteal region) and 1 oral location (inner buccal region) upon arrival of the donor at the unit. Samples obtained from donors PM03–PM012 were stored at –20 °C before epithelial isolation.

After manual removal of the subcutaneous/submucosal fat, the epithelial layer was isolated using an enzymatic method, which included 4 h incubation in a 2.5 mg/mL Dispase II solution in PBS at 37 °C on a shaker plate. The epithelium was then carefully peeled away from the thicker dermis layer and circular punch biopsies (diameter 5 mm) were obtained from this thin epithelial layer (for technical reasons this procedure was reversed for PM03–PM12: first punch biopsies, then isolation). For 3 samples (i.e., 1E, 4N and 14N) larger tissue biopsies were obtained from remnant tissues. As the total biopsy surface is hard to determine for these samples, they were excluded from clone size inference.

DNA was extracted from the resulting epithelial tissue discs using the QIAamp DNA Micro Kit. Briefly, 100 µl of lysis buffer was added to each 5 mm punch biopsy and subjected to lysis using the TissueLyser II (Qiagen), at speed of 30 Hz for 90 s. DNA was isolated according to the manufacturer's protocol and DNA concentrations and quality were measured using NanoDrop 1000 (Thermo Fisher Scientific). DNA integrity was determined by agarose gel electrophoresis, with Hind III Digested lambda DNA (N3012S, NEB) loaded as a molecular marker.

Deep targeted sequencing. A gene panel of 153 genes was developed for this study: 101 driver genes, 20 housekeeping genes and 32 immune genes (Table S1). The 101 driver genes included 76 genes used in an earlier study on healthy skin⁴, completed with 25 genes from Cosmic Cancer Gene Census³⁹ (v91, tier 1, somatic mutations) that have been related to skin or head and neck cancer. The 20 housekeeping genes were randomly selected from a list of 3804 previously reported genes that shown uniform expression across a panel of tissues⁴⁰. Only genes with no previous association with cancer, as curated manually from literature, were withheld. The 32 immune genes belong to MHC pathways or have been associated with immune evasion by previous studies^{8,31,41–44} (Table S1). Custom baits, targeting the coding region of the gene panel, were designed using the Agilent SureDesign software on the most recent human genome build (hg38). The total size of the target regions was 566 kbp. Deep (1000×) targeted paired-end DNA nanoball sequencing (DNBseq)⁴⁵ was performed by BGI genomics using the exome capture methodology.

Genome alignment and somatic mutation calling. Paired-end reads (100 bp read length) were aligned to the GRCh38.p13 human reference genome using BWA-mem2⁴⁶, BAM files from 2 different sequencing runs (lanes) were merged using Samtools⁴⁷ and PCR duplicates were removed using Picard's MarkDuplicates (<http://broadinstitute.github.io/picard/>). Somatic mutations were called using the *ShearwaterML* algorithm, available in the *deepSNV* R Package⁴. *ShearwaterML* uses a position-specific maximum-likelihood approach to call low frequency mutations from deep targeted sequencing data by comparing each sample to a set of reference samples from the same individual. The approach was applied to each sample in this study, using samples from other locations from the same donor as a reference set. Only bases with a Phred quality score > 30 were analyzed to minimize the impact of sequencing errors. Mutations were detected at $P_{adj} < 0.05$ and annotated using ANNOVAR⁴⁸. All somatic mutations located within 10 base pairs from each other were flagged for manual curation using Integrative Genomics Viewer (IGV)⁴⁹ to check whether they occurred on the same read. If applicable, they were reannotated as DNVs, multinucleotide substitutions or deletions.

dN/dS calculations. The ratio of non-synonymous to synonymous mutations per site (i.e., dN/dS) was calculated globally for all genes or groups of genes (driver genes, immune genes, housekeeping genes, as described higher) and individually for each gene as described previously⁵⁰:

$$\frac{dN}{dS} = \frac{\eta_s}{\sum_i N_i P_i / \sum_i S_i P_i}$$

with $i \in \{A[C > A]A, \dots, T[T > G]T\}$ (96 substitution classes)

where n is defined as the number of observed non-synonymous mutations (across all analyzed skin or oral samples), s as the number of observed synonymous mutations, N_i and S_i as the number of non-synonymous and synonymous sites with class i substitutions (trinucleotide substitution types) and P_i as the probability of substitution class i. Probabilities were derived from the frequencies of the 96 trinucleotide substitution classes in skin melanoma (SKCM; skin samples) and head and neck squamous skin cancer data (HNSC; oral samples), available from The Cancer Genome Atlas (TCGA, <https://portal.gdc.cancer.gov/>). A one-sided binomial test was used to check whether dN/dS ratios were significantly higher than 1. Genes were considered under positive selection when adjusted P values (P_{adj} ; Benjamini Hochberg method) were lower than 0.1.

A related (sub)metric was calculated for missense and nonsense mutations separately by replacing the observed (n) and expected (N) number of non-synonymous mutations by the number of missense (dMiss/dS) or nonsense (dNons/dS) mutations in the formula above.

PolyPhen-2 scores. PolyPhen-2 (PP2) scores were calculated for each mutation using ANNOVAR⁴⁸. For each gene (or group of genes), the scores were then compared to the expected PP2 scores, calculated from 100,000 random point mutations sampled in the same gene, with prior probabilities given by the TCGA SKCM (skin samples) or HNSC (oral samples) datasets using a one-sided Wilcoxon rank sum test.

Clone size inference. Mutational clone sizes (surface area) were estimated from the VAF using the following formula:

$$\text{Clone size}(\text{mm}^2) = 2 \times \text{VAF} \times \text{total biopsy size}(\text{mm}^2)$$

With the total biopsy size = 19.63 mm² for 5 mm diameter punch biopsies.

Healthy skin and SCC somatic mutation data. Healthy skin⁴ and SCC²⁷ mutation data were downloaded from the supplementary tables provided by the authors of the respective studies. Variants were reannotated and PP2 scores added to both datasets using ANNOVAR. Genomic coordinates were converted from hg19 to hg38 using UCSC's liftOver⁵¹ if required.

Mutational signatures. The contribution of each known COSMIC SBS mutational signature to our dataset was estimated using the R Bioconductor package *MutSignatures* (function *resolveMutSignatures*)⁵².

SiMSen sequencing. To detect and quantify 2 UV-specific hot spot mutations (Table S1), we applied SiMSen-Seq (Simple, Multiplexed, PCR-based barcoding of DNA for Sensitive mutation detection using Sequencing) as described previously²⁴. Sequencing was performed on an Illumina MiniSeq instrument in 150 bp single-end mode. Raw FastQ files were subsequently processed using a modified version of Debarcer⁵³. For the *RPL13A* (chr19: 49,487,384–49,487,466) and *DPH3* (chr3: 16,264,961–16,265,030) promoter amplicons, sequence reads containing the barcode were grouped into barcode families. Barcode families with at least 10 reads, where all of the reads were identical (or ≥ 90% for families with > 20 reads), were required to compute consensus reads.

Code and data availability. The targeted sequencing data that support the results reported in this study is available at the European Genome–Phenome Archive (EGA; <https://ega-archive.org>; accession number EGAD00001008956), which is hosted by the European Bioinformatics Institute (EBI) and the Centre for Genomic Regulation (CRG). Due to ethical and legal reasons, the data is deposited under controlled access. Data use conditions attached to this EGA dataset limit its use to approved users at a specific institution for a specific a health/medical/biomedical project and dictate that useful results should be made available to the wider scientific community. Access requests should be addressed to Jimmy Van den Eynden (jimmy.vandeneynden@ugent.be).

Code and downstream data used to produce the results described in this manuscript are available on GitHub at <https://github.com/CCGGLab/mutClon>.

Data processing and statistical analysis. The R statistical package (v4.0) was used for all data processing and statistical analysis. Details on the statistical tests used in this study are reported in the respective sections. *P* values less than 0.05 were considered significant for individual tests. For multiple comparisons, false discovery rate (FDR) corrections were performed using the Benjamini–Hochberg method.

Received: 2 March 2022; Accepted: 3 June 2022

Published online: 20 June 2022

References

1. Vogelstein, B. *et al.* Cancer genome landscapes. *Science* **339**, 1546–1558 (2013).
2. Gerstung, M. *et al.* The evolutionary history of 2,658 cancers. *Nature* **578**, 122–128 (2020).
3. Jonason, A. S. *et al.* Frequent clones of p53-mutated keratinocytes in normal human skin. *Proc. Natl. Acad. Sci. U. S. A.* **93**, 14025–14029 (1996).
4. Martincorena, I. *et al.* Tumor evolution. High burden and pervasive positive selection of somatic mutations in normal human skin. *Science* **348**, 880–886 (2015).
5. Martincorena, I. *et al.* Somatic mutant clones colonize the human esophagus with age. *Science* **362**, 911–917 (2018).
6. Yokoyama, A. *et al.* Age-related remodelling of oesophageal epithelia by mutated cancer drivers. *Nature* **565**, 312–317 (2019).
7. Lee-Six, H. *et al.* The landscape of somatic mutation in normal colorectal epithelial cells. *Nature* **574**, 532–537 (2019).
8. Nanki, K. *et al.* Somatic inflammatory gene mutations in human ulcerative colitis epithelium. *Nature* **577**, 254–259 (2020).
9. Lac, V. *et al.* Oncogenic mutations in histologically normal endometrium: The new normal?. *J. Pathol.* **249**, 173–181 (2019).
10. Suda, K. *et al.* Clonal expansion and diversification of cancer-associated mutations in endometriosis and normal endometrium. *Cell Rep.* **24**, 1777–1789 (2018).
11. Brunner, S. F. *et al.* Somatic mutations and clonal dynamics in healthy and cirrhotic human liver. *Nature* **574**, 538–542 (2019).
12. Ng, S. W. K. *et al.* Convergent somatic mutations in metabolism genes in chronic liver disease. *Nature* **598**, 473–478 (2021).
13. Yoshida, K. *et al.* Tobacco smoking and somatic mutations in human bronchial epithelium. *Nature* **578**, 266–272 (2020).
14. Lawson, A. R. J. *et al.* Extensive heterogeneity in somatic mutation and selection in the human bladder. *Science* **370**, 75–82 (2020).

15. Li, R. *et al.* Macroscopic somatic clonal expansion in morphologically normal human urothelium. *Science* **370**, 82–89 (2020).
16. Tomasetti, C. Mutated clones are the new normal. *Science* **364**, 938–939 (2019).
17. Martincorena, I. Somatic mutation and clonal expansions in human tissues. *Genome Med.* **11**, 1–3 (2019).
18. Colom, B. *et al.* Spatial competition shapes the dynamic mutational landscape of normal esophageal epithelium. *Nat. Genet.* **52**, 604–614 (2020).
19. Colom, B. *et al.* Mutant clones in normal epithelium outcompete and eliminate emerging tumours. *Nature* **598**, 510–514 (2021).
20. Vijg, J. & Dong, X. Pathogenic mechanisms of somatic mutation and genome mosaicism in aging. *Cell* **182**, 12–23 (2020).
21. Jaiswal, S. & Ebert, B. L. Clonal hematopoiesis in human aging and disease. *Science* **366**, eaan4673 (2019).
22. Waerlop, F., Rashidian, N., Marrannes, S., D’Herde, K. & Willaert, W. Thiel embalmed human cadavers in surgical education: Optimizing realism and long-term application. *Am. J. Surg.* **221**, 1300–1302 (2021).
23. Valcke, B. *et al.* Screening algorithms for HBV, HCV, HIV and syphilis in an anatomical donation program. *Ann. Anat. Anat. Anz.* **239**, 151805 (2022).
24. Fredriksson, N. J. *et al.* Recurrent promoter mutations in melanoma are defined by an extended context-specific mutational signature. *PLoS Genet.* **13**, e1006773 (2017).
25. Elliott, K. *et al.* Elevated pyrimidine dimer formation at distinct genomic bases underlies promoter mutation hotspots in UV-exposed cancers. *PLoS Genet.* **14**, e1007849 (2018).
26. Kakiuchi, N. & Ogawa, S. Clonal expansion in non-cancer tissues. *Nat Rev Cancer* <https://doi.org/10.1038/s41568-021-00335-3> (2021).
27. Chang, D. & Shain, A. H. The landscape of driver mutations in cutaneous squamous cell carcinoma. *npj Genomic Med.* **6**, 61 (2021).
28. Schleicher, K. & Schramek, D. AJUBA: A regulator of epidermal homeostasis and cancer. *Exp. Dermatol.* **30**, 546–559 (2021).
29. Li, M. *et al.* Somatic mutations in the transcriptional corepressor gene BCORL1 in adult acute myelogenous leukemia. *Blood* **118**, 5914–5917 (2011).
30. Mologni, L. *et al.* Concomitant BCORL1 and BRAF mutations in vemurafenib-resistant melanoma cells. *Neoplasia* **20**, 467–477 (2018).
31. Rooney, M. S., Shukla, S. A., Wu, C. J., Getz, G. & Hacohen, N. Molecular and genetic properties of tumors associated with local immune cytolytic activity. *Cell* **160**, 48–61 (2015).
32. McGranahan, N. *et al.* Allele-specific HLA loss and immune escape in lung cancer evolution. *Cell* **171**, 1259–1271.e11 (2017).
33. van den Eynden, J., Jiménez-Sánchez, A., Miller, M. L. & Larsson, E. Lack of detectable neoantigen depletion signals in the untreated cancer genome. *Nat. Genet.* **51**, 1741–1748 (2019).
34. De Hertog, S. A. *et al.* Relation between smoking and skin cancer. *J. Clin. Oncol.* **19**, 231–238 (2001).
35. Li, R. *et al.* A body map of somatic mutagenesis in morphologically normal human tissues. *Nature* **597**, 398–403 (2021).
36. Bizzotto, S. *et al.* Landmarks of human embryonic development inscribed in somatic mutations. *Science* **371**, 1249–1253 (2021).
37. Park, S. *et al.* Clonal dynamics in early human embryogenesis inferred from somatic mutation. *Nature* **597**, 393–397 (2021).
38. Coorens, T. H. H. *et al.* Extensive phylogenies of human development inferred from somatic mutations. *Nature* **597**, 387–392 (2021).
39. Forbes, S. A. *et al.* COSMIC: Somatic cancer genetics at high-resolution. *Nucleic Acids Res.* **45**, D777–D783 (2017).
40. Eisenberg, E. & Levanon, E. Y. Human housekeeping genes, revisited. *Trends Genet.* **29**, 569–574 (2013).
41. Tucci, M. *et al.* Immune system evasion as hallmark of melanoma progression: The role of dendritic cells. *Front. Oncol.* **9**, 1148 (2019).
42. de Sanctis, F., Ugel, S., Facciponte, J. & Facciabene, A. The dark side of tumor-associated endothelial cells. *Semin. Immunol.* **35**, 35–47 (2018).
43. Paul, P. *et al.* A genome-wide multidimensional RNAi screen reveals pathways controlling MHC class II antigen presentation. *Cell* **145**, 268–283 (2011).
44. Leone, P. *et al.* MHC class I antigen processing and presenting machinery: organization, function, and defects in tumor cells. *JNCI J. Natl. Cancer Inst.* **105**, 1172–1187 (2013).
45. Porreca, G. J. Genome sequencing on nanoballs. *Nat. Biotechnol.* **28**, 43–44 (2010).
46. Vasimuddin, Md., Misra, S., Li, H. & Aluru, S. Efficient Architecture-Aware Acceleration of BWA-MEM for Multicore Systems. in *2019 IEEE International Parallel and Distributed Processing Symposium (IPDPS)* 314–324 (IEEE, 2019). <https://doi.org/10.1109/IPDPS.2019.00041>.
47. Danecek, P. *et al.* Twelve years of SAMtools and BCFtools. *Gigascience* **10**, giab008 (2021).
48. Wang, K., Li, M. & Hakonarson, H. ANNOVAR: functional annotation of genetic variants from high-throughput sequencing data. *Nucleic Acids Res* **38**, e164 (2010).
49. Robinson, J. T., Thorvaldsdóttir, H., Wenger, A. M., Zehir, A. & Mesirov, J. P. Variant review with the integrative genomics viewer. *Can. Res.* **77**, e31–e34 (2017).
50. van den Eynden, J. & Larsson, E. Mutational signatures are critical for proper estimation of purifying selection pressures in cancer somatic mutation data when using the dN/dS metric. *Front. Genet.* **8**, 74 (2017).
51. Rosenbloom, K. R. *et al.* The UCSC genome browser database: 2015 update. *Nucleic Acids Res* **43**, D670–681 (2014).
52. Fantini, D., Vidimar, V., Yu, Y., Condello, S. & Meeks, J. J. MutSignatures: an R package for extraction and analysis of cancer mutational signatures. *Sci. Rep.* **10**, 18217 (2020).
53. Stahlberg, A. *et al.* Simple, multiplexed, PCR-based barcoding of DNA enables sensitive mutation detection in liquid biopsies using sequencing. *Nucleic Acids Res.* **44**, e105–e105 (2016).

Acknowledgements

This work was supported by the Ghent University Special Research Fund Starting Grant (JvdE; BOF STG.2019.0073.01), Kom op tegen Kanker (Stand up to Cancer), the Flemish cancer society (TL; STI. VLK.2022.0002.01) and Barncancer (JTS; TJ2021-0068). We thank all collaborators from the human Anatomy and Embryology unit at Ghent University for their daily technical and administrative support. Lastly, our deepest gratitude and thoughts are reserved for the donors and their families.

Author contributions

J.V.d.E designed the study. J.V.d.E. and T.L. performed the bioinformatics analysis and drafted the manuscript. W.W. was responsible for donor medical record screening and inclusion and supervised donor sampling. J.V.d.V. developed the donor sampling method. A.V. and E.B. developed and performed the epithelial isolation procedure. J.S. was responsible for DNA extraction, concentration measurements and integrity checks. E.L. and K.E. performed the SiMSen sequencing. All authors read and approved the manuscript.

Competing interests

The authors declare no competing interests.

Additional information

Supplementary Information The online version contains supplementary material available at <https://doi.org/10.1038/s41598-022-14240-8>.

Correspondence and requests for materials should be addressed to J.V.d.E.

Reprints and permissions information is available at www.nature.com/reprints.

Publisher's note Springer Nature remains neutral with regard to jurisdictional claims in published maps and institutional affiliations.



Open Access This article is licensed under a Creative Commons Attribution 4.0 International License, which permits use, sharing, adaptation, distribution and reproduction in any medium or format, as long as you give appropriate credit to the original author(s) and the source, provide a link to the Creative Commons licence, and indicate if changes were made. The images or other third party material in this article are included in the article's Creative Commons licence, unless indicated otherwise in a credit line to the material. If material is not included in the article's Creative Commons licence and your intended use is not permitted by statutory regulation or exceeds the permitted use, you will need to obtain permission directly from the copyright holder. To view a copy of this licence, visit <http://creativecommons.org/licenses/by/4.0/>.

© The Author(s) 2022